



HAL
open science

Improved modeling of Mars' HDO cycle using a Mars' Global Climate Model

Margaux Vals, Loïc Rossi, Franck Montmessin, Franck Lefèvre, Francisco Gonzalez-Galindo, Anna Fedorova, Mikhail Luginin, François Forget, Ehouarn Millour, Oleg Korablev, et al.

► To cite this version:

Margaux Vals, Loïc Rossi, Franck Montmessin, Franck Lefèvre, Francisco Gonzalez-Galindo, et al.. Improved modeling of Mars' HDO cycle using a Mars' Global Climate Model. *Journal of Geophysical Research. Planets*, 2022, 127 (8), pp.e2022JE007192. 10.1029/2022JE007192 . insu-03740754

HAL Id: insu-03740754

<https://insu.hal.science/insu-03740754>

Submitted on 31 Jul 2022

HAL is a multi-disciplinary open access archive for the deposit and dissemination of scientific research documents, whether they are published or not. The documents may come from teaching and research institutions in France or abroad, or from public or private research centers.

L'archive ouverte pluridisciplinaire **HAL**, est destinée au dépôt et à la diffusion de documents scientifiques de niveau recherche, publiés ou non, émanant des établissements d'enseignement et de recherche français ou étrangers, des laboratoires publics ou privés.

Improved modeling of Mars' HDO cycle using a Mars' Global Climate Model

Margaux Vals¹, Loïc Rossi¹, Franck Montmessin¹, Franck Lefèvre¹, Francisco Gonzalez-Galindo², Anna Fedorova³, Mikhail Luginin³, François Forget⁴, Ehouarn Millour⁴, Oleg Korablev³, Alexander Trokhimovskiy³, Alexey Shakun³, Antoine Bierjon⁴, Luca Montabone⁵

¹LATMOS/IPSL, UVSQ Université Paris-Saclay, Sorbonne Université, CNRS, Guyancourt, France

²Instituto de Astrofísica de Andalucía-CSIC (IAA), Granada, Spain

³Space Research Institute (IKI), Moscow, Russia

⁴Laboratoire de Météorologie Dynamique/IPSL, Sorbonne Université, ENS, PSL Research

University, Ecole Polytechnique, CNRS, Paris France

⁵Space Science Institute, Boulder, CO, USA

Key Points:

- The HDO cycle has been implemented in the last version of the LMD Mars GCM including microphysics and radiative effect of water ice clouds.
- Kinetics effect is now included in HDO fractionation during condensation and proves to be significant.
- Supersaturation, the presence of which is regulated by cloud processes, alters significantly the relative abundances of HDO and H₂O.

Corresponding author: Margaux Vals, margaux.vals@latmos.ipsl.fr

Abstract

HDO and the D/H ratio are essential to understand Mars past and present climate, in particular with regard to the evolution through ages of the Martian water cycle. We present here new modeling developments of the HDO cycle with the LMD Mars GCM. The present study aims at exploring the behaviour of the D/H ratio cycle and its sensitivity to the modeling of water ice clouds and the formulation of the fractionation by condensation. Our GCM simulations are compared with observations provided by the Atmospheric Chemistry Suite (ACS) on board the ESA/Roscosmos Trace Gas Orbiter, and reveal that the model quite well reproduces the temperature and water vapor fields, which offers a good basis for representing the D/H ratio cycle. The comparison also emphasizes the importance of modelling the effect of supersaturation, resulting from the microphysical processes of water ice clouds, to correctly account for the water vapor and the D/H ratio of the middle-to-upper atmosphere. This work comes jointly with a detailed comparison of the measured D/H profiles by TGO/ACS and the model outputs, conducted in the companion paper of Rossi et al. 2022 (this issue).

Plain Language Summary

The D/H ratio observed in a planetary atmosphere is traditionally used as a proxy to estimate the initial water reservoir of the planet. We present here an improved global circulation model including HDO, the main isotope of water on Mars. The updated model takes into account the details of the formation of clouds and their radiative effect. It also includes the effect of photochemistry on HDO and deuterated species. We find that supersaturation is key to the representation of the D/H cycle by making the hygropause more porous, allowing more HDO in the upper atmosphere. It also reduces the efficiency of the isotopic fractionation occurring at condensation. We present here comparisons between observations by the ACS spectrometer onboard the orbiter TGO. While the model is globally in agreement with the observations, the inability of the model to reproduce the observed vertical distribution of dust, especially during the Global Dust Storm, cause discrepancies in the representation of water vapour. The model reveals the importance of representing the process of supersaturation to correctly account for the water vapor amount reaching the top of the atmosphere and estimate the D/H ratio at escape.

1 Introduction

The D/H ratio is commonly used to constrain the amount of water that was present initially on Mars. Because the light hydrogen atom escapes more easily to space than deuterium, the D/H ratio of the martian atmosphere is 5 to 6 times higher than the Earth's oceans (Owen et al., 1988; Encrenaz, T. et al., 2018; Krasnopolsky, 2015; Villanueva et al., 2015). This is often viewed as a testimony of a progressive loss of water that has made its heavier isotope accruing over time. Furthermore, the D and H atoms populating the exosphere, where they can escape, are initially produced from their precursors H₂O and HDO in the lower atmosphere. H₂O tends to be preferentially photolysed, because of its lower absorption cross-section (Cheng et al., 1999), while HDO is preferentially condensed because of its lower vapor pressure (Bertaux & Montmessin, 2001). These isotopic-dependent processes reduce the ability of deuterium to access the upper atmosphere, and thus its escape rate in comparison to hydrogen.

Deciphering the main mechanisms that control the D/H cycle on Mars is key to understanding how escape has affected the evolution of water on the planet. The recent martian missions provide new insights into this problematic by profiling for the first time D/H ratio (Vandaele et al., 2019; Chaufray et al., 2021; Alday et al., 2021a; Villanueva et al., 2021). In addition, numerical models complete the investigation by helping to interpret the physical processes observed.

In this paper, we refine the modeling of the HDO cycle that was initially developed by Montmessin et al. (2004), and recently re-implemented in the current version of the Martian Global Climate Model (GCM) of the Laboratoire de Météorologie Dynamique (LMD) by Rossi et al. (2021). This work is part of the perspective of a detailed analysis of the D/H ratio behavior based on model outputs and TGO/ACS observations (see companion paper Rossi et al. 2022, this issue).

Condensation-induced fractionation, used in Rossi et al. (2021), makes the HDO cloud cycle mainly dependent on H₂O cloud formation. Cloud formation is a key feature of the H₂O cycle, in particular, microphysics and radiative effect of water ice clouds have been shown to be essential to physically reproduce the observed water cycle with the LMD GCM (Madeleine et al., 2012; Navarro et al., 2014). Microphysics comprise nucleation, ice growth and scavenging of dust. Modeling these different processes allows supersaturation to build up in the model. A phenomenon that is known to exist in the atmosphere of Mars (Maltagliati et al., 2011; Fedorova et al., 2020; Belyaev et al., 2021). Also, radiative effect of water ice clouds have been shown to play a crucial role in the temperature field and, consequently, in the global circulation. In this paper we incorporate a HDO cloud formation model into a GCM including microphysics and radiative effect of clouds, and study the impact on the HDO and D/H cycles. Within the fractionation by condensation, we also implement the effect of kinetics, which moderates the HDO condensation reaction depending on the saturation conditions. To make our model consistent with the detailed analysis of the D/H cycle observed by TGO/ACS (see companion paper Rossi et al. 2022, this issue), we compare the model outputs to TGO/ACS temperature, water vapor and saturation data in the extreme conditions of the MY34 Global Dust Storm.

Section 2 describes the model. Section 3 describes the upgrades implemented for the modeling of the HDO cycle. Section 4 analyzes the results obtained with the new simulations. Section 5 confronts the model outputs of the water cycle in comparison to TGO/ACS observations. Section 6 discusses the results in comparison to TGO/ACS observations and the consequences for the D/H cycle. Section 7 summarizes the conclusions of the paper and proposes perspectives of this work.

2 Description of the model

2.1 General

The model used in this paper is the Martian Global Climate Model (GCM) developed at the Laboratoire de Météorologie Dynamique (LMD) in collaboration with several European teams (LATMOS, IAA Granada, University of Oxford, The Open University) (Forget et al., 1999). A detailed overview of the model, including the last implementations regarding the dust and water cycles, is provided by Navarro et al. (2014). Nevertheless, a brief description of the main modeling features of these two cycles is given in the following paragraphs.

Airborne dust is represented by a two-moment scheme, i.e. by two atmospheric tracers, accounting for both the dust particle number mixing ratio and the dust mass mixing ratio (Madeleine et al., 2011). The effective radius of the dust particles is then derived from these two moments assuming a log-normal distribution. The dust tracers are incorporated into to a "semi-interactive" scheme (Madeleine et al., 2011), which simultaneously allows the free evolution of the vertical distribution of dust, going through the different physical parametrizations, and ensures the match of the integrated column dust opacity to the observed values, as compiled by Montabone et al. (2015); Montabone et al. (2020), for the radiative transfer calculations.

The atmospheric water is represented by two tracers, accounting for the ice and vapor mixing ratios. The implementation of the radiative effect of water ice clouds (Madeleine et al., 2012), shown to have a major impact on the global circulation, has led to the need to finer represent the processes of cloud formation. A microphysics scheme, adapted from Montmessin et al. (2002), has been introduced in the model by Navarro et al. (2014) and includes the main processes of nucleation, ice growth and scavenging, allowing the occurrence of supersaturation. The cloud particles are represented by both the amount of condensed water, i.e. the mass mixing ratio of water ice, and the dust particles on which the water has condensed, i.e. the dust particles converted to Cloud Condensation Nuclei (CCN). As for the dust particles, the CCNs follow a two-moment scheme, with their own size distribution, as described in Navarro et al. (2014).

2.2 Modeling of the HDO cycle

The HDO cycle based on the model developed by Montmessin et al. (2004), has been introduced in the most recent version of the GCM Rossi et al. (2021), yet without activating the radiative effect of clouds and the microphysics scheme. We briefly remind the main features of this implementation.

HDO is represented in the model by two tracers, namely its vapor and ice phases. Both tracers of the isotope go through the same physics of the model as the water tracer, and are freely mixed from the surface to the top of the model. The HDO initial atmospheric and surface mixing ratio are imposed in the model with a ratio of $5 \times \text{VSMOW}$. The effect of fractionation by condensation has been introduced in the model presented by Rossi et al. (2021), based on the calculation of a fractionation factor depending on the temperature according to the empirical expression of Lamb et al. (2017):

$$\alpha(T) = \frac{(HDO/H_2O)_{ice}}{(HDO/H_2O)_{vap}} = \exp\left(\frac{13525}{T^2} - 5.59 \times 10^{-2}\right) \quad (1)$$

The condensing mass flux dM_D of HDO can then be expressed from the condensing mass flux dM_H of H_2O as:

$$dM_D = \alpha(T)dM_H \times \frac{M_D}{M_H} \quad (2)$$

where M indicates the mass mixing ratio in the vapor phase, with subscript H referring to water and D to HDO. Finally, as described in Rossi et al. (2021), in the dynamical

146 part of the model, the isotopic ratio instead of the HDO tracer itself is advected to en-
 147 sure monotonicity (Risi et al., 2010).

148 **3 Upgrades in modeling the HDO cycle**

149 **3.1 HDO combined with microphysics of water ice clouds**

150 In the study of Rossi et al. (2021), the choice was made to use the same simplified
 151 cloud model version as in Montmessin et al. (2004). It means the radiative effect of wa-
 152 ter ice clouds was neglected, as were the details of cloud microphysics (nucleation, ice
 153 growth and scavenging), which are necessary to account for supersaturation. In the present
 154 paper, we focus on the impact of using the current, detailed, cloud model of Navarro et
 155 al. (2014) on the HDO cycle. In practice, it requires to apply the equation (2) on the wa-
 156 ter condensing mass flux computed at each microphysical timestep.

157 **3.2 Implementation of the effect of kinetics on the fractionation by con- 158 densation**

159 Condensation fractionation is complicated by kinetics. Indeed, the higher weight
 160 of the isotope HDO restricts its molecular mobility and therefore its ability to diffuse in
 161 a gaseous environment compared to H₂O. The molecular diffusion coefficient is a key pa-
 162 rameter of the condensation flow. If condensation is not fast enough to maintain an equi-
 163 librium between the phases, i.e. to maintain saturation condition, kinetics then signif-
 164 icantly affect fractionation. In the experimental framework described by Merlivat and
 165 Nief (1967), the vapor to ice conversion is slow enough for the system to remain perma-
 166 nently close to equilibrium, and hence, to isotopic equilibrium. However, ice formation
 167 in nature does not necessarily occur in isotopic equilibrium. For example, terrestrial po-
 168 lar ice clouds encounter conditions in which the condensing vapor must diffuse in a strongly
 169 supersaturated air (120 % relative humidity, Jouzel and Merlivat (1984)). In situ titra-
 170 tions of deuterium in ice clearly showed that the effect of actual fractionation was not
 171 reproduced by Equation (1) (Jouzel & Merlivat, 1984). This formulation had to include
 172 the effect of kinetics. Once taken into account, this correction makes it possible to ob-
 173 tain a valid relation under real conditions, where the kinetic fractionation coefficient α_c
 174 is expressed in function of the fractionation coefficient of the isotopic equilibrium, ob-
 175 tained with Equation (1), and the ratio of saturation of water vapor S :

$$176 \quad \alpha_c = \frac{\alpha S}{\alpha(D_{H_2O}/D_{HDO})(S-1) + 1} \quad (3)$$

177 Where D_{H_2O} and D_{HDO} are the coefficients of diffusion of respectively H₂O and HDO.
 178 The HDO flux is then calculated as in equation 2 with α_c instead of α .

179 **3.3 Photochemistry of HDO**

180 The photodissociation of HDO has been implemented in the latest version of the
 181 photochemical module coupled to the LMD GCM, described in Lefèvre et al. (2021). The
 182 HDO absorption cross-sections considered in the model are those measured at 295 K by
 183 Cheng et al. (2004) (125-140 nm) and Chung et al. (2001) (140-195 nm). The HDO cross-
 184 section is assumed to be identical to that of H₂O shortward of 125 nm.

185 The process of photolysis is particularly important from around 40 to 60 km alti-
 186 tude. HDO presents a lower absorption cross section to solar UV, which preserves HDO
 187 from photolysis relative to H₂O and thus refrains the release of Deuterium atoms. The
 188 model also disposes of a vertical extension up to the exobase around 250 km and fully
 189 represents the photochemical reactions occurring at these altitude ranges (Angelats i Coll
 190 et al., 2005; González-Galindo et al., 2013). This part was completed with the photo-

191 chemical reactions of the deuterated species, both in the neutral and ionized form, based
 192 on Yung et al. (1988).

193 4 Model results and sensitivity

194 GCM simulations presented in this section have all been run with a horizontal res-
 195 olution of 64×48 grid points, corresponding to $\sim 5.625^\circ$ resolution in longitude at the
 196 equator and $\sim 3.75^\circ$ resolution in latitude, and 32 vertical levels. The vertical resolu-
 197 tion irregularly decreases from ~ 2 m close to the surface, to correctly resolve the plan-
 198 etary boundary layer, to ~ 5 km close to the top of the model located around 120 km al-
 199 titude. For the study described in this section, photochemistry and the extension to the
 200 thermosphere introduced in Section 3.3, are not included, as they are computationally
 201 expensive. Their effect will nevertheless be studied and discussed in Sections 5 and 6.
 202 The D/H ratio of both the atmosphere and the surface ice have been initialized to the
 203 value of $5 \times$ VSMOW. The dust load scenario used in the simulations corresponds to the
 204 "climatology" one, typical for a martian year without a global dust storm. The initial
 205 state for the presented simulations has been obtained after 10 Martian years of simula-
 206 tion in which the HDO modeling upgrades presented in Section 3, i.e. radiatively active
 207 clouds, microphysics and kinetics, were activated. In this section, we focus on the par-
 208 ticular season of perihelion, around $L_s = 270^\circ$, for the comparison between the differ-
 209 ent simulations. This season is the most challenging in modeling as it corresponds to the
 210 dust storm season, and is particularly critical for the hydrogen escape as emphasized in
 211 Alday et al. (2021b). All Figures of the Section display the fields during daytime (local
 212 time 14:00), when the altitude of the hygropause is supposed to be the highest and es-
 213 cape rate the most efficient.

214 4.1 Effect of radiatively active clouds and microphysics on the D/H cy- 215 cle

216 In this section we study the separate impact of radiatively active clouds (RAC) and
 217 of microphysics on the D/H cycle. In particular, supersaturation, which is the main con-
 218 sequence of using improved microphysics, is analyzed. Figure 1 shows the zonal mean
 219 of temperature, water vapor superimposed with water ice contours, and D/H ratio of the
 220 vapor phase superimposed with the seasonal stream functions, at the Southern Hemi-
 221 sphere Summer solstice $L_s = 270^\circ$ and at local time 14:00 for three cases of simulation:
 222 one with all processes activated (RAC, microphysics and kinetics), which is referred to
 223 as the reference simulation ([REF]), and two other simulations, where RAC and super-
 224 saturation have been alternately deactivated (respectively called [RAC OFF] and [su-
 225 persat OFF] ; see details on how we perform this simulation in Section 4.1.2), all other
 226 parameters being equal. Figure 2 shows the difference between the different fields of the
 227 different simulations, including a fourth simulation corresponding to the initial case of
 228 simple physics of clouds used in Rossi et al. (2021) (simulation called "simple", for "sim-
 229 ple physics of clouds").

230 4.1.1 Impact of RAC

231 We analyse the difference observed between simulations [REF] and [RAC OFF] to
 232 isolate the effect of radiatively active clouds on the D/H cycle. Differences between the
 233 two simulations are depicted by Figures 2a, 2b and 2c. During daytime (here at local
 234 time 14:00), the main effect of adding the RAC is the warming of the middle atmosphere
 235 between 10 and 1 Pa at the low to mid-latitudes, and at the high latitudes (enhanced
 236 polar warming). The consequence of such an increase of temperature is the enhancement
 237 of the global circulation, illustrated by the streamfunctions shown in Figures 1c and 1f.
 238 This effect was already reported in Madeleine et al. (2012) and Navarro et al. (2014).
 239 Both effects of increasing temperature and enhancing circulation impact the water cy-

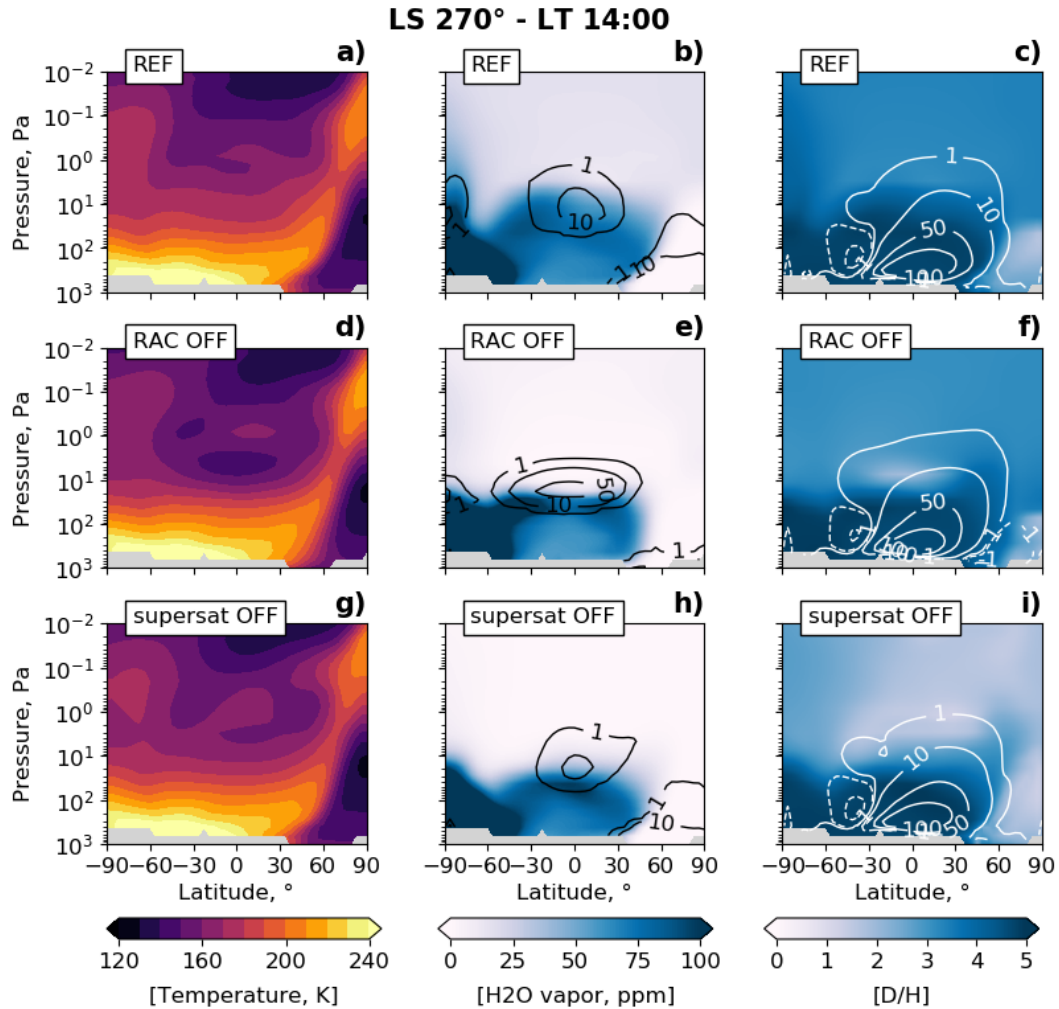


Figure 1. Meteorological variables output of the model zonally averaged at LT=14:00 around $L_s = 270^\circ$ [REF] Results for the reference GCM simulation with radiative effect and microphysics of clouds. [RAC OFF] Results for the GCM simulation in which radiative effect of clouds is turned off. [supersat OFF] Results of the GCM simulation in which the supersaturation has been turned off. (Left column) Temperature (K). (Middle column) H₂O ice mixing ratio (ppm). (Right column) D/H ratio of the vapor phase. White contours are the stream function in 10^8 kg s^{-1} averaged over $L_s = 240^\circ - 270^\circ$.

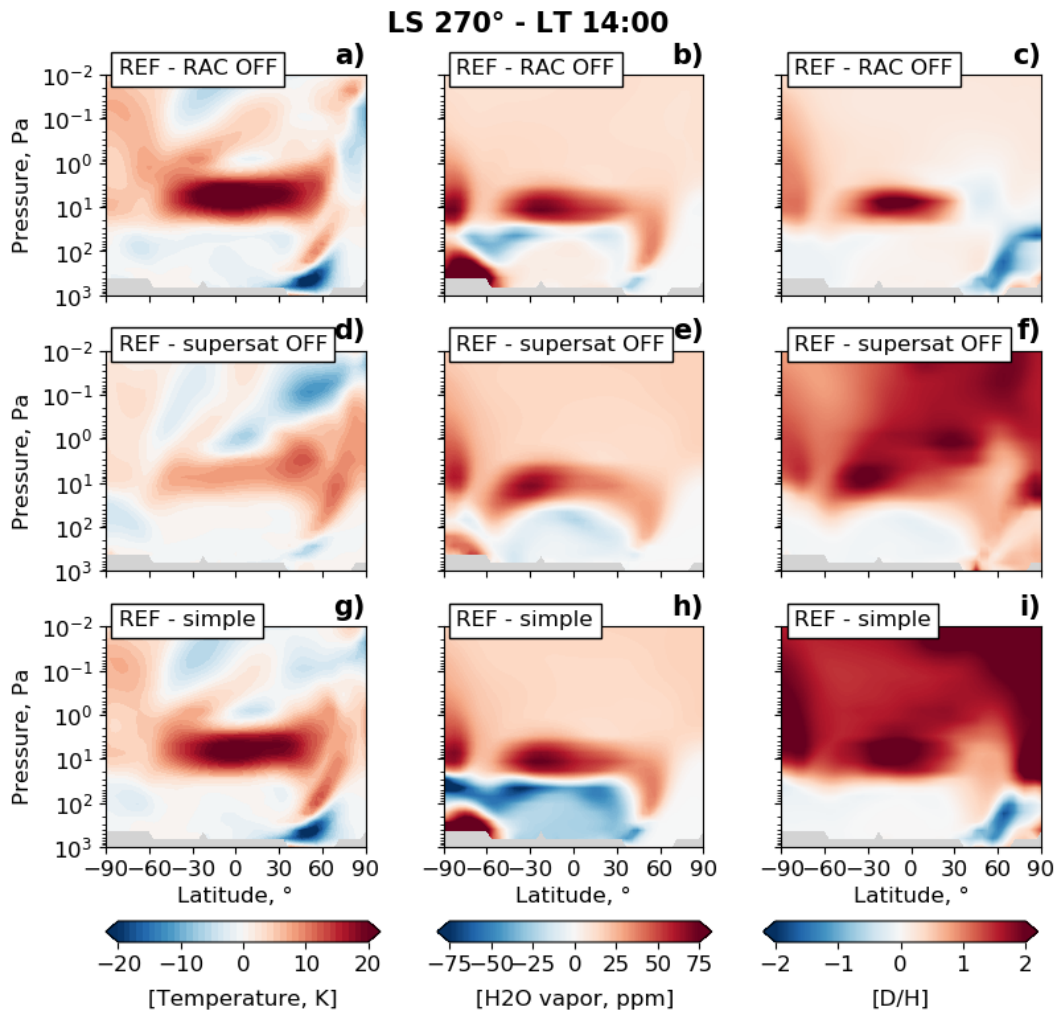


Figure 2. Meteorological variables output of the model zonally averaged at LT=14:00 around $L_s = 270^\circ$ [REF -RAC off] Difference between the meteorological fields of the GCM simulation [REF] and the GCM simulation [RAC OFF]. [REF - supersat OFF] Difference between the meteorological fields of the GCM simulation [REF] and the GCM simulation [supersat OFF]. [REF -simple] Difference between the meteorological fields of the GCM simulation [REF] and the GCM simulation run with simple physics of clouds, i.e. deactivated radiative effect and microphysics [simple]. (Left column) Difference of temperature (K). (Middle column) Difference of the H₂O vapor mixing ratio (ppm). (Right column) Difference of D/H ratio of the vapor phase. Panel c) also displays the contours of saturation in the case of the simulation [REF].

240 cle, on the one hand by rising the hygropause altitude, and, on the other hand, by fos-
 241 tering the distribution of water higher in the atmosphere. The concentration of water
 242 vapor is increased by ~ 50 ppm at the hygropause in the low-to-middle latitudes, so as
 243 in the South pole near to the surface, and by ~ 20 ppm in average in the atmosphere above
 244 the hygropause. The concentration of ice clouds is decreased by $\sim 20\%$ around 10 Pa in
 245 the middle atmosphere at low-to-middle latitudes. These ice clouds also show a differ-
 246 ent structure, spanning a wider altitude range and centered to the tropics, instead of be-
 247 ing spread over all latitudes in [RAC OFF]. More water ice (tens of ppm) is also observed
 248 in [REF] at the North Pole. The D/H ratio is increased by two in the middle altitudes
 249 between 10 and 1 Pa, where the temperature increase and the cloud depletion are ob-
 250 served. The radiative effect of clouds tends to warm the atmosphere between 10 and 1 Pa,
 251 which impedes condensation and thus fractionation and explains the corresponding higher
 252 D/H ratio of the vapor phase. However, a slightly lower D/H ratio is observed at higher
 253 altitude in the area of the polar warming and of the Northern pole. This can be inferred
 254 from the presence of thicker ice clouds in [REF] than in [RAC OFF] seen in the North
 255 pole, which create a stronger fractionation in these latitudes and a lower amount of HDO
 256 in the vapor phase.

257 **4.1.2 Impact of microphysics and the particular role of supersaturation**

258 The implementation of microphysics in the LMD GCM has been shown to signif-
 259 icantly improve the representation of the water cycle by correcting unrealistic biases am-
 260 plified by the radiative effect of clouds (Madeleine et al., 2012; Navarro et al., 2014). In
 261 particular, microphysics now allow supersaturation to exist and build up, which is key
 262 to simulate clouds realistically (Navarro et al., 2014; Maltagliati et al., 2011; Urata &
 263 Toon, 2013). Indeed, microphysics of clouds involve the conversion of dust to conden-
 264 sation nuclei, and the release of this dust in the atmosphere right below the cloud level
 265 where water ice particles fall and then sublime. Nucleation and condensation depend
 266 on the availability of dust nuclei and the formation of clouds may be inhibited by a pre-
 267 vious episode of scavenging that left condensation level devoid of nuclei. Thus the model
 268 is now able to reproduce the emergence and further growth supersaturation, which is ob-
 269 served in the martian atmosphere (Maltagliati et al., 2011; Fedorova et al., 2020). In this
 270 part, we focus on the particular role of the presence of supersaturation in the altitude
 271 dependence of D/H. In order not to be biased by the radiative effect of clouds, which can-
 272 not be correctly represented without activating microphysics, we chose to isolate the ef-
 273 fect of supersaturation with a simulation called [supersat OFF]. In this simulation, clouds
 274 are still formed with detailed microphysics, including the physical processes of nucleation
 275 and ice particle growth, but in the end of each time step, the remnants of supersaturated
 276 water vapor are systematically turned into ice. As the number of CCN is however con-
 277 served, particles get instantaneously bigger and fall rapidly by sedimentation to the sur-
 278 face. This way, the impact of supersaturation on the altitude dependence of D/H can
 279 be addressed.

280 Results are shown in Figures 2d, 2e and 2f, which correspond to the difference of
 281 temperature, water vapor and D/H ratio between the [REF] and [supersat OFF] sim-
 282 ulations at $L_s=270^\circ$ and local time 14:00. The temperature field displays an enhanced
 283 polar warming effect in the case of [REF] in comparison to [supersat OFF], as shown by
 284 2d). This difference can be inferred from the clouds, which impact on the circulation:
 285 the water ice issued from the conversion of supersaturated water vapor in the case of [su-
 286 persat OFF] involve bigger particles, which fall rapidly to the surface. Therefore, atmo-
 287 spheric water ice is less present in [supersat OFF] than in [REF], i.e. clouds are thin-
 288 ner (see Figures 1b and 1h) and have less radiative impact on the global circulation, which
 289 reduces polar warming. Figure 2e reveals that water vapor is redistributed from the lower
 290 to the middle-to-upper altitudes in the case of permitted supersaturation, explaining the
 291 higher amount (increase by 10 to 50 ppm) predicted in the middle-to-upper atmosphere
 292 at all latitudes from around 100 Pa altitude, so as the depletion observed in the lower

293 altitude ranges. The hygropause is lower in the case of [supersat OFF] and water vapor
 294 is confined to lower altitude ranges than in [REF]. The difference in D/H between sim-
 295 ulations replicates that of water vapor (see Figure 2e vs. Figure 2f). The global effect
 296 of supersaturation at the perihelion season makes the hygropause and the deuteropause
 297 more porous, and allows more water vapor to penetrate the middle-to-upper atmosphere
 298 while inhibiting fractionation by condensation. Microphysics, especially supersaturation,
 299 significantly impact water vapor and ice distributions, which in turn affects the D/H struc-
 300 ture essentially by allowing water with a high D/H ratio to migrate towards high alti-
 301 tude.

302 **4.1.3 Impact of RAC and microphysics**

303 Finally we analyse the difference between simulations [REF] and [simple], consid-
 304 ering the impact of both effects of microphysics and radiatively active clouds (see Fig-
 305 ures 2g, 2h and 2i for the differences between both simulations). The global effect for
 306 temperature is almost the same as the difference between simulation [REF] and [RAC
 307 OFF]: there is a strong warming at the same locations (see Figure 2g). The water con-
 308 centration is increased the same way as in the difference between simulation [REF] and
 309 [supersat OFF], redistributing water through a more porous and higher hygropause (see
 310 Figure 2h). The difference in the D/H ratio illustrates well the combination of both ef-
 311 fects with the local increase of D/H around 10 Pa and the increase of D/H in the up-
 312 per atmosphere (see Figure 2i). This illustrates the impact of both physical processes
 313 of microphysics and radiative effect of clouds on the D/H cycle through the impact on
 314 the temperature and the water cycle. Both effects significantly impact the distribution
 315 of water in the atmosphere, and consequently significantly impact the D/H ratio.

316 **4.2 Effect of the kinetics on the D/H cycle**

317 Taking into account the effect of kinetics in the calculation of the condensation flux
 318 of HDO makes the fractionation effect directly dependent on supersaturation. This ef-
 319 fect is illustrated by Figure 3, where the HDO vapor mass mixing ratio, and the D/H
 320 ratio are displayed respectively for the reference simulation ([REF]) and a simulation in
 321 which the effect of kinetics has been turned off ([kinetics OFF]). Kinetics counterbalance
 322 fractionation by condensation, as HDO diffuses slower than H₂O in the condensing flux.
 323 Equation 2 says that for a given temperature, the higher the saturation, the lower the
 324 fractionation coefficient. The correlation between the D/H ratio and the saturation is
 325 well illustrated by the contours of saturation showed in Figure 3i.

326 The global impact of kinetics on the integrated D/H column is shown in Figure 4.
 327 The main impact is in the polar nights, where the supersaturation is high. The high frac-
 328 tionation effect occurring at these locations is clearly reduced by kinetics, increasing the
 329 D/H from 3 to 4×SMOW.

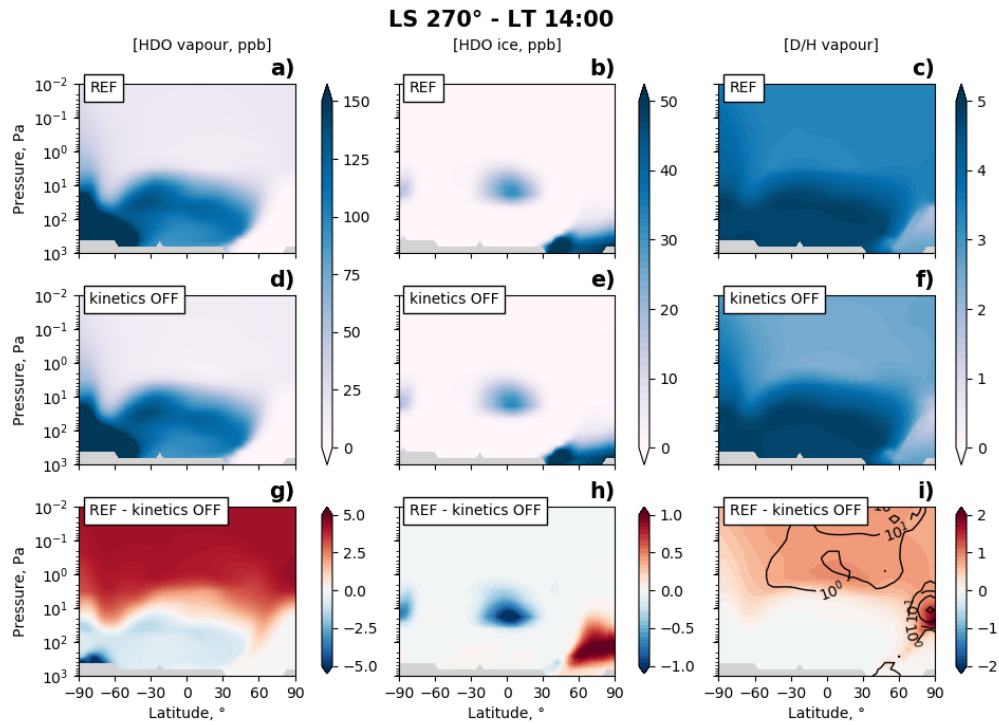


Figure 3. Model outputs of the zonally averaged HDO vapor, HDO ice and D/H at LT=14:00 around $L_s = 270^\circ$ [REF] Results for the reference GCM simulation with radiative effect and microphysics of clouds. [kinetics OFF] Results for the GCM simulation in which the effect of kinetics off fractionation has been turned on. [REF - kinetics OFF] Difference between the two simulations [REF] and [kinetics OFF] described before. (Left column) HDO vapor mixing ratio (ppb). (Middle column) HDO ice mixing ratio (ppb). (Right column) D/H ratio of the vapor phase. The contours of saturation are displayed in the sub-figure i (black contours)

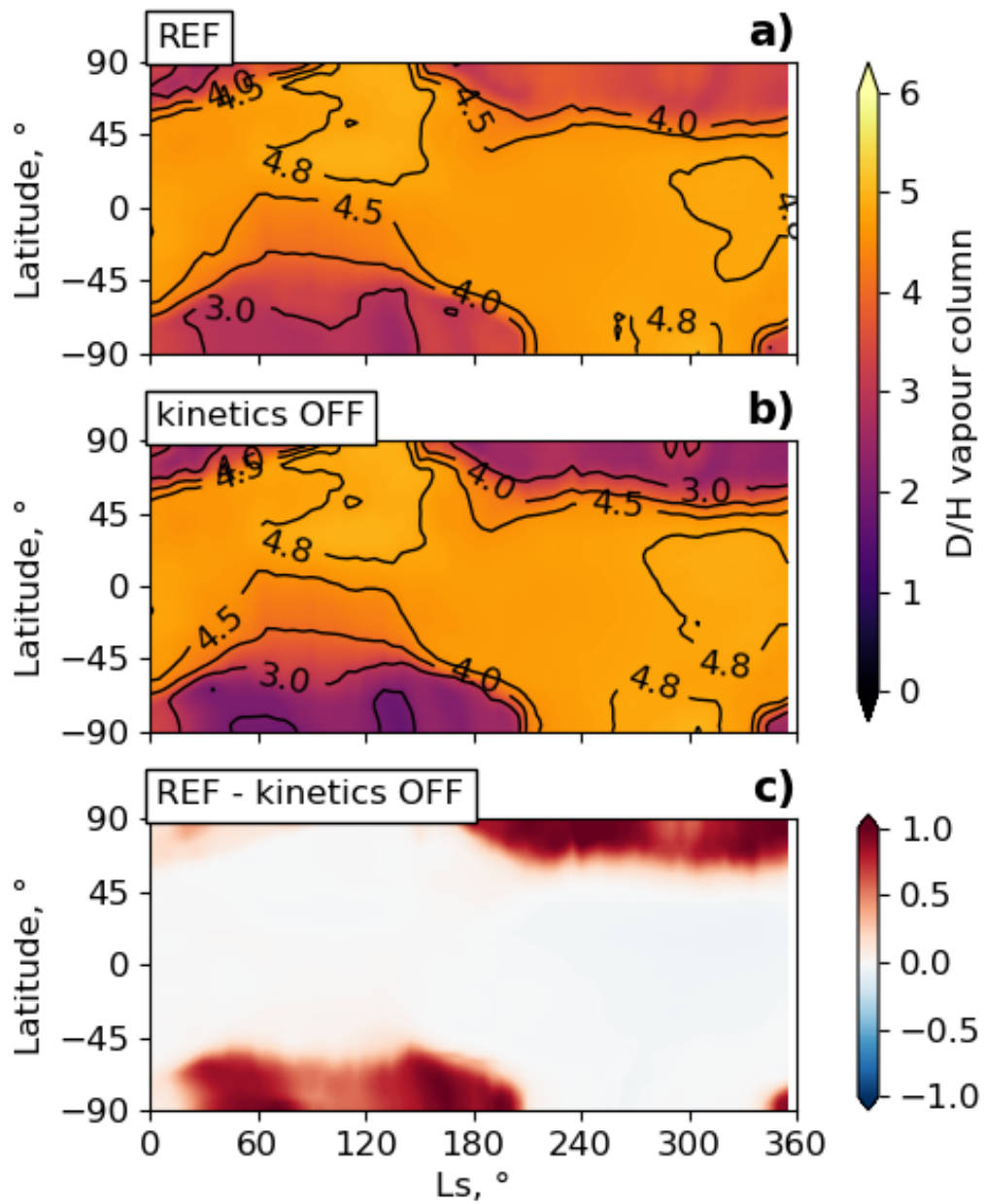


Figure 4. [REF] Zonal average of the D/H integrated water vapor column for the reference GCM simulation with radiative effect, microphysics of clouds and the effect of kinetics on fractionation. [kinetics ON] Zonal average of the D/H integrated water vapor column for the GCM simulation in which the effect of kinetics on fractionation has been turned on. [kinetics ON -REF] Difference between the two simulations [kinetics ON] and [REF] described before.

330 **5 Comparison with observations**

331 In this section, we confront our reference simulation in which all the upgrades of
 332 the HDO modeling presented before have been activated, to temperature, H₂O and sat-
 333 uration occultation profiles derived from the TGO/ACS instrument provided by A. Fe-
 334 dorova for the MY34 with the NIR channel (Fedorova et al., 2020). This comparison aims
 335 at assessing the validity of the model regarding water and condensation. A detailed com-
 336 parison between model and observations for HDO is conducted in Rossi et al. 2022 com-
 337 panion paper (this issue).

338 As mentioned in Navarro et al. (2014) in Section 4.3, the supersaturated water present
 339 above the hygropause is exposed to photodissociation, which cannot be neglected in this
 340 case. Therefore, the photochemistry module described by Lefèvre et al. (2021), includ-
 341 ing the upgrades implemented for Deuterium (see Section 3.3), so as the extension to ther-
 342 mosphere, have been turned on in the simulations presented in this section, in order to
 343 make the most realistic comparison to the observations. The model outputs, for a sim-
 344 ulation run with the MY34 dust scenario of Montabone et al. (2020), have been extracted
 345 and interpolated at the same L_s , spatial coordinates (latitude, longitude) and local times
 346 as the ACS data. Both, model outputs and data, were interpolated on a vertical grid of
 347 101 levels of 1 km resolution from 0 to 100 km above the areoid.

348 **5.1 Temperature**

349 Figure 5 compares the temperature field produced by TGO/ACS for both hemi-
 350 spheres during MY34 between $L_s = 150^\circ$ and $L_s = 360^\circ$ with the GCM.

351 The global structure of temperature is overall well reproduced by the model. The
 352 model is generally warmer than observations in the upper atmosphere above 50 km in
 353 both hemispheres. The temperature field remains warmer even in the model for the case
 354 of simple cloud physics without radiative effect of clouds (not shown here), suggesting
 355 that it is not linked to cloud formation but to other processes.

356 The comparison with data from the instrument Mars Climate Sounder onboard Mars
 357 Reconnaissance Orbiter (MRO/MCS), provided by L. Montabone, and shown in Figure
 358 6, confirms the warm bias of 20 K, in particular in the higher latitudes and upper alti-
 359 tudes. This bias could be explained by processes not included in the model. For instance,
 360 some simulations have shown that taking into account non-orographic gravity waves can
 361 reduce the global circulation and, consequently, the polar warming (Gilli et al., 2020).
 362 The influence of the CO₂ clouds microphysics, studied with the model in a paper recently
 363 submitted by A. Määttänen, is also a factor to be explored, as it could impact the south-
 364 ward returning circulation in the lower atmosphere.

365 **5.2 Water vapor**

366 Figure 7 is the same as Figure 5 but for the H₂O vapor field. As for the temper-
 367 ature, the global structure of the water distribution, including the average altitude of
 368 the hygropause, is well reproduced by the model. However, the model presents slightly
 369 more water vapor in the upper atmosphere than what is observed, in particular in the
 370 northern hemisphere between $L_s = 210^\circ$ and $L_s = 240^\circ$, whereas it fails to reproduce
 371 the distinct increase of water vapor between $L_s = 270^\circ$ and $L_s = 300^\circ$ in the south-
 372 ern hemisphere.

373 The excess of water does not necessarily correlate with the warm temperature bias.
 374 Indeed, the difference in water vapor persists in the particular cases where the measured
 375 and the modelled temperature finely agree, mainly in the tropical latitudes, like for in-
 376 stance near to $L_s = 240^\circ$ (Figures 8a, 8b and 8c), where saturation is much higher in
 377 the model than in the observations. In other cases, as the one displayed in Figures 8c,

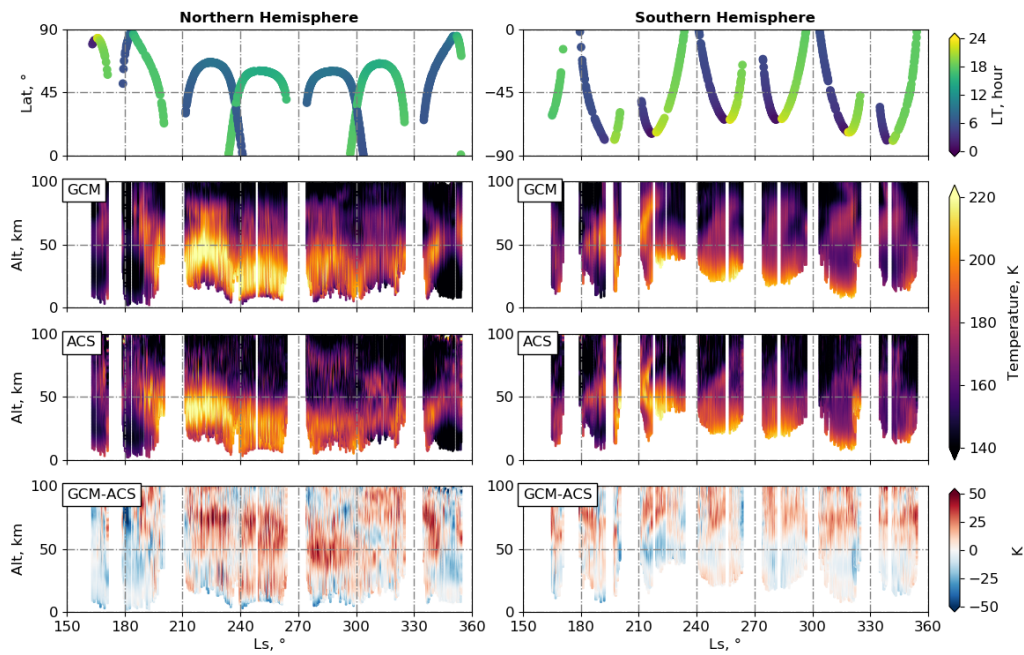


Figure 5. GCM temperature profiles interpolated to the ACS spatial and temporal coordinates, as a function of altitude and solar longitude (L_s). Left column: northern hemisphere, right column: southern hemisphere. First panel corresponds to the data coverage in latitude and local time. Second panel displays the GCM outputs. Third panel shows the ACS data. Fourth panel is the difference between the GCM outputs and the ACS data.

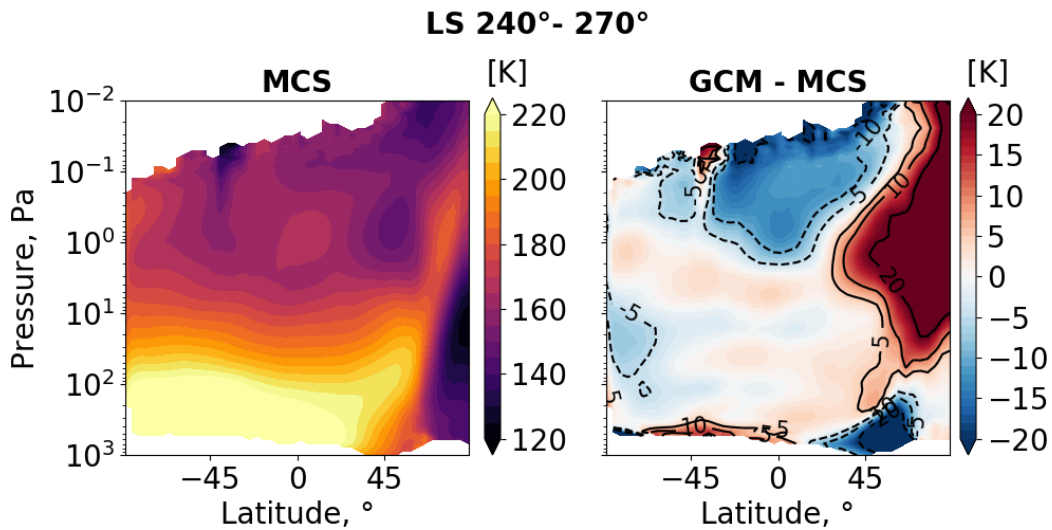


Figure 6. Comparison between the zonal mean daytime temperature at $\sim L_s = 240^\circ$ as measured by MCS and as computed by the GCM. Left panel: MCS temperature field as a function of pressure and latitude, right panel: difference between the GCM outputs and the MCS data.

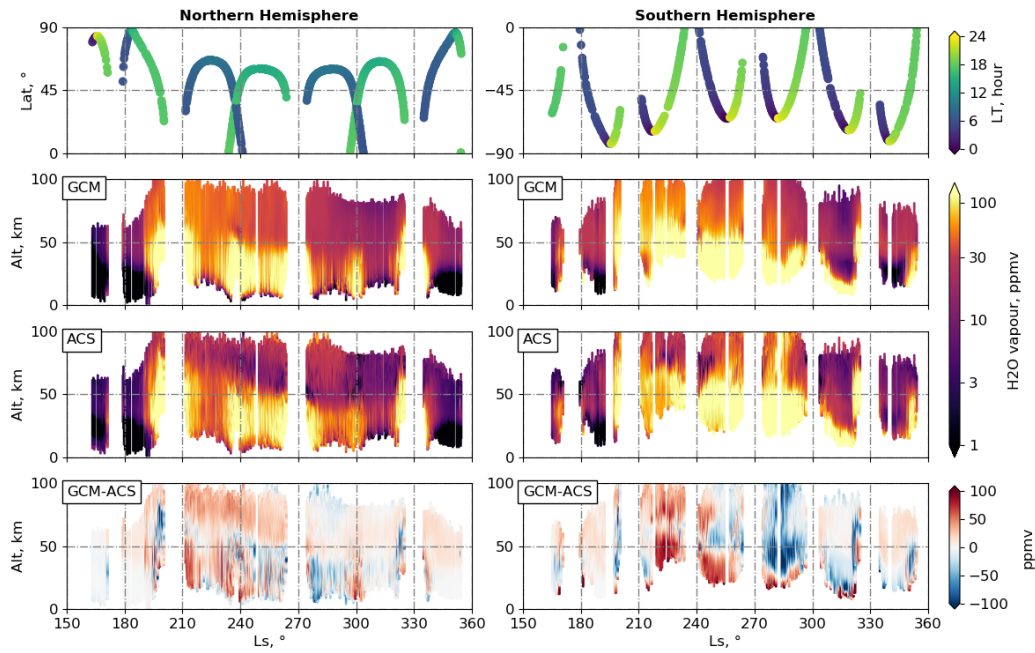


Figure 7. Same layout as Figure 5 but for water vapor volume mixing ratio

378 8d and 8e, the disagreement in water vapor seems related to the differences in temper-
 379 ature. In this Figure we see that the peak of 300 ppm of water vapor between 40 and
 380 50 km doesn't correspond to supersaturated conditions, but to a slight increase of tem-
 381 perature in the same altitude range.

382 For both types of profiles presented here, the observed discrepancies between obser-
 383 vations and model outputs could be explained by the difficulty of the model to repro-
 384 duce the dust vertical distribution, in particular during the Global Dust Storm. For or-
 385 bit 3418 ($L_s = 240.0^\circ$, $\text{Lat}=11.3^\circ$, $\text{LT}=6.3$ h), shown in 8a, 8b and 8c, the underesti-
 386 mation of condensation, correlated with the excess of supersaturation, could be the re-
 387 sult of a lack of dust nuclei in the upper atmosphere. Indeed, ACS observations have iden-
 388 tified the presence of water ice clouds at altitudes as high as 80km (Stcherbinine et al.,
 389 2020), which are not reproduced by the model. This is also illustrated by Figure 9a that
 390 compares GCM outputs with TGO/ACS/TIRVIM and TGO/ACS/NIR ice mass data
 391 around the same ranges of solar longitude and latitude as the profile 3418 (Luginin et
 392 al., 2020). We can see that the model does not reproduces the water ice amount observed
 393 between 60 and 100 km altitude.

394 For orbit 4192 ($L_s = 279.9^\circ$, $\text{Lat}=-62.4^\circ$, $\text{LT}=1.8$ h), shown in 8d, 8e and 8f, the
 395 layer of warmer temperature observed around 30 to 50 km by ACS, that is also corre-
 396 lated to much higher water vapor mixing ratio, could be the result of detached dust lay-
 397 ers created by strong convective activity (Spiga et al., 2013; Daerden et al., 2015; Heav-
 398 ens et al., 2011; Wang et al., 2018; Heavens et al., 2019). In the model, which does not
 399 account for these subgrid-scale processes, water vapor is concentrated to lower altitude
 400 than observed while the lower hygro-pause prevents water from reaching higher altitude.
 401 This hypothesis is corroborated by Figure 9b which compares GCM outputs with MRO/MCS
 402 dust opacity which shows that the dust opacity observed is not well reproduced by the
 403 model.

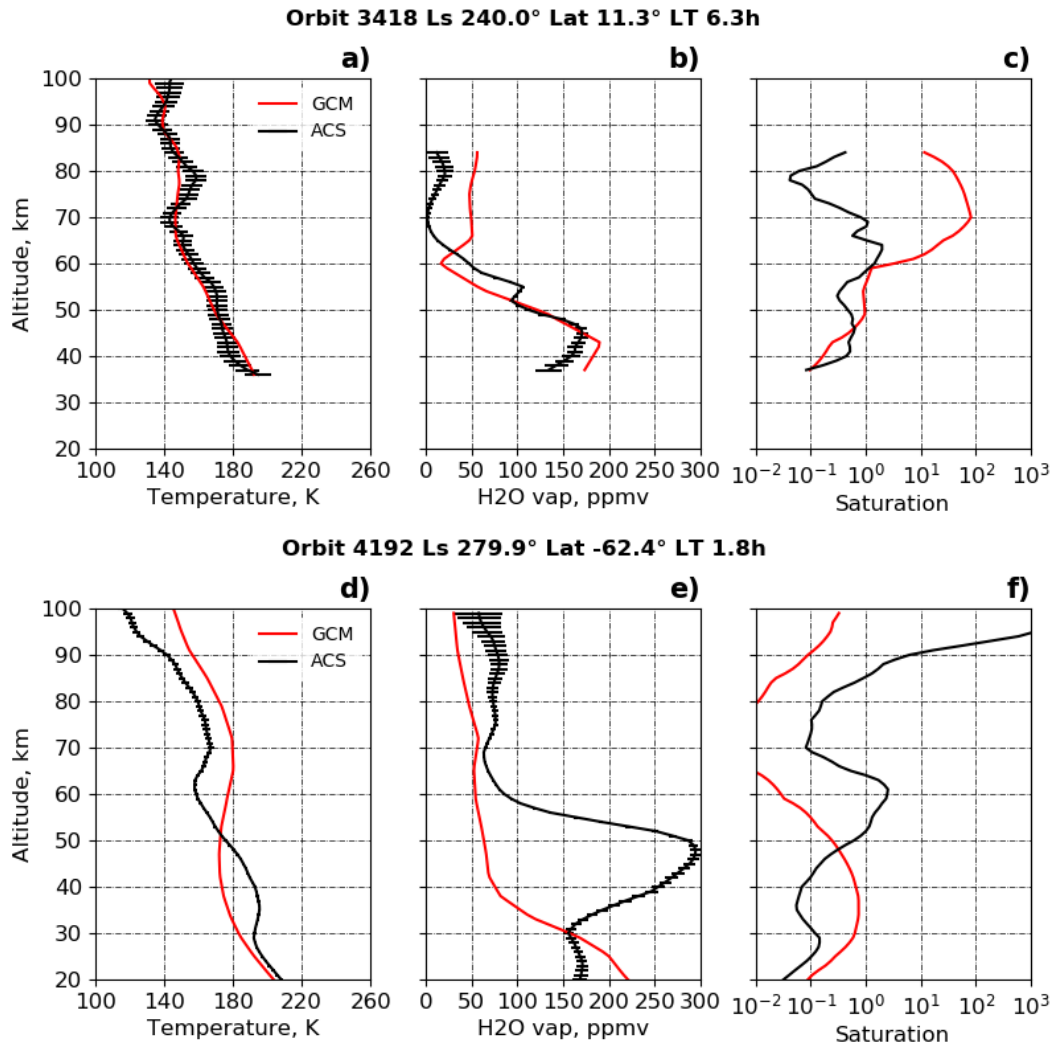


Figure 8. Profiles of temperature, water vapor mixing ratio and saturation in function of altitude corresponding to orbits 3418 ($L_s=240.0^\circ$, $Lat=11.3^\circ$, $LT=6.3$ h) and 4192 ($L_s=279.9^\circ$, $Lat=-62.4^\circ$, $LT=1.8$ h) as measured by ACS (black line) and computed by the GCM (red line).

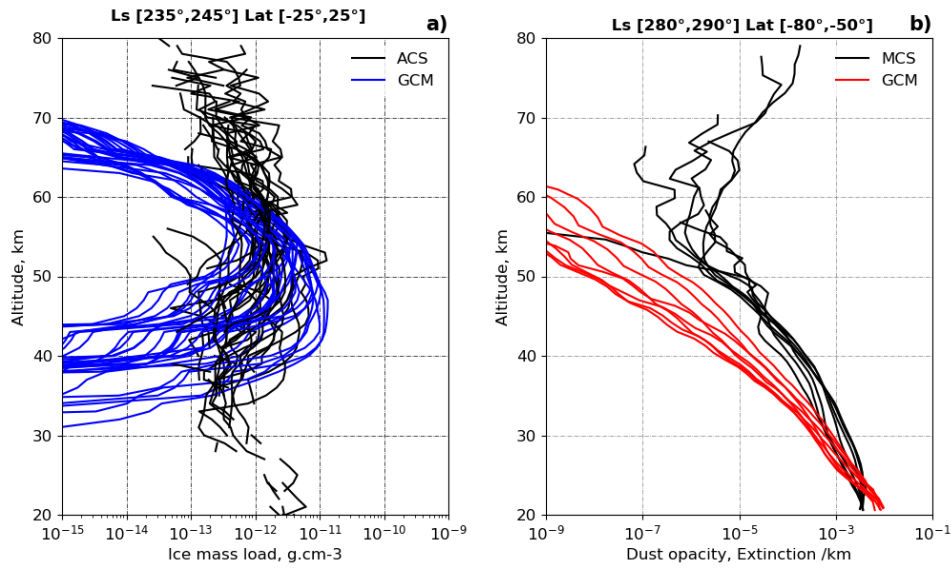


Figure 9. a) Profiles of water ice mass load between $L_s = 235^\circ$ and $L_s = 245^\circ$ and latitude 25°S and 25°N as measured by ACS (black line) and computed by the GCM (blue line). b) Profiles of nighttime dust opacity extinction at wavelength $21.6 \mu\text{m}$ between $L_s=280^\circ$ and $L_s=290^\circ$ and latitude 60°S and 90°N as measured by MCS (black line) and computed by the GCM (red line).

404

5.3 Saturation

405

406

407

408

409

410

411

412

413

414

Figure 10 is the same as Figure 5 but for the saturation field. As for temperature and water vapor, the GCM reproduces the main features of supersaturation observed. However, some disagreements appear and globally correlate with the ones observed in the upper atmosphere (above 50 km) for the water vapor. From $L_s = 210^\circ$ to $L_s = 270^\circ$, saturation in the model is higher than in the observations near 100 km, and from $L_s = 270^\circ$ to $L_s = 300^\circ$ in the Northern Hemisphere. However, observations present higher saturation from 50 to 100 km altitude, which correlates with the colder temperatures. In the Southern Hemisphere, the lack of water vapor seen in the model in comparison with observations between $L_s = 270^\circ$ and $L_s = 300^\circ$ correlates with the lower saturation observed in comparison to TGO/ACS data.

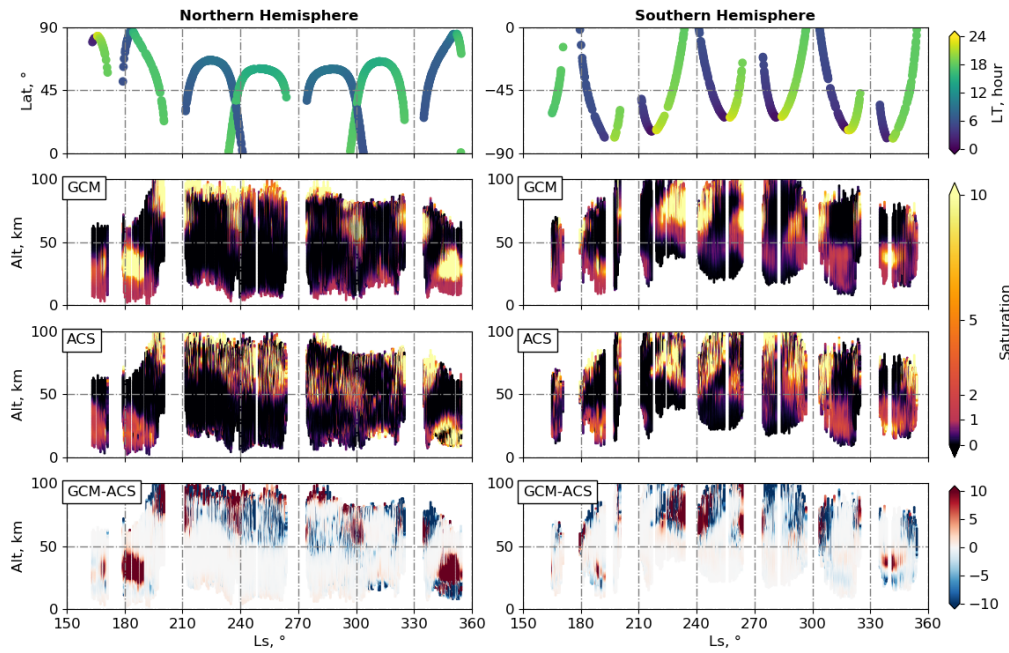


Figure 10. Same layout as Figure 5 but for the saturation

6 Discussion

6.1 Impact of the different physical processes

Figure 11 summarizes the impact of each different physical process implemented in the model and studied in this work. It shows the H_2O and HDO mixing ratios, and the D/H ratio at 80 km altitude, as computed by the model, and interpolated at the ACS measurements coordinates, for a simulation of reference [REF], where all physical packages (RAC, microphysics, kinetics and photochemistry) have been activated, i.e. the simulation used for the comparison with observations in Section 5, and for other experimental simulations, in which each physical process studied has been separately turned off. The impact on D/H of each physical process is detailed hereafter.

As illustrated in Section 4, radiatively active clouds contribute to the presence of water vapor at high altitude. The comparison between [REF] (red dots) and [RAC OFF] (green dots) in Figure 11 reveals that ignoring the radiative effect of clouds significantly degrades the agreement between the model and the observations. Indeed, the amount of water vapor can vary by one ($L_s = 210^\circ - 270^\circ$), to two orders of magnitude ($L_s = 270^\circ - 330^\circ$) from one simulation to the other. This also has a consequence on the HDO mixing ratio, and on the D/H ratio, which is depleted for the simulation [REF] at 80 km altitude in comparison to simulation [RAC OFF]. This can possibly be explained by the North pole water ice clouds, which are thicker in [REF] than in [RAC OFF] at this season, as illustrated by Figure 2 in Section 4.1.1. The formation of these clouds in [REF] impoverishes the air in deuterium through the global circulation, which results in a lower D/H ratio in the upper atmosphere in comparison to [RAC OFF].

Supersaturation significantly impacts D/H. The comparison between simulations [REF] (red dots) and [supersat OFF] (blue dots) in Figure 11 reveals that ignoring supersaturation results in an underestimation of water vapor of two orders of magnitude

440 in comparison to the ACS measurements. This proves supersaturation cannot be neglected
 441 to realistically reproduce the water amount in the upper atmosphere. This also has a
 442 strong impact on D/H, which can be two times lower in the case of not allowing the su-
 443 persaturation ([SUPERSAT OFF]) than in [REF]. Indeed, according to the model, wa-
 444 ter vapor in the middle-to-upper atmosphere is in a supersaturated state. Supersatura-
 445 tion makes the hygropause, and the deuteropause more porous, and allows H₂O as well
 446 as HDO, penetrate higher altitude ranges than the ones delimited by the water ice cloud
 447 level. Both H₂O and HDO amounts increase by two orders of magnitude at 80 km when
 448 supersaturation is enabled, as shown by Figure 11. Water can then reach the middle-
 449 to-upper atmosphere and becomes exposed to photolysis, subsequently determining the
 450 D/H ratio at escape. We also notice that the representation of supersaturation allows
 451 the presence of water (tens of ppm) within the middle-to-upper atmosphere as soon as
 452 $L_s = 190^\circ$, at the beginning of the storm. There we could have expected that the model,
 453 which fails at reproducing the vertical distribution of dust, would not be able to trans-
 454 port water at such high altitudes. This is the case in the model presented by Neary et
 455 al. (2020), where supersaturation is not taken into account. Therefore, allowing super-
 456 saturation compensates partly for the misrepresentation of the dust dynamics.

457 The effect of kinetics in the fractionation process is illustrated by Figure 11 with
 458 simulations [REF] (red dots) and [kinetics OFF] (purple dots). As this effect only inter-
 459 venes in HDO fractionation, it does not impact on the comparison of water vapor be-
 460 tween the model and the observations (red and purple dots are almost superimposed).
 461 As expected, the difference is seen in the mixing ratio of HDO, and consequently in the
 462 D/H ratio, which is globally increased by 5% when this process is taken into account.

463 The comparison between simulations [REF] (red dots) and [photochemistry OFF]
 464 (orange dots) in the same figure shows that ignoring photochemistry significantly degrades
 465 the agreement between model and observations. This is especially seen within $L_s = 270^\circ -$
 466 330° , where the amount of water vapor is decreased by 25 to 50 % when activating pho-
 467 tochemical reactions in both hemispheres. The photolysis is expected to be significant
 468 at these altitudes, and is particularly strong near to the perihelion (Clarke et al., 2014;
 469 Alday et al., 2021a). The global impact of photochemistry at this altitude is to increase
 470 D/H ratio. As H₂O is preferentially photolysed compared to HDO, the D/H ratio of the
 471 neutral species is increased. The effect is particularly important around $L_s=315^\circ$ in both
 472 hemispheres, where a peak is observed for [REF] and not for [photochemistry OFF]. These
 473 peaks indicate a particularly strong photolysis activity, which can be the result of sam-
 474 pling the descending air from the thermosphere (Hadley circulation near the equinox and
 475 the poles), where photolysis is particularly active.

476 6.2 Global average versus ACS sampling

477 Considering that ACS sampling is restricted by the TGO orbit which induces a lat-
 478 tudinal drift with time, it is important to question the global representativity of such
 479 sampling. This kind of question can be addressed with the model which simulates the
 480 entire Martian globe and allows comparing the state of the atmosphere at the sampling
 481 locations with the state of the global atmosphere. One expects a bias in this configura-
 482 tion, but does it make ACS and TGO incapable of delivering a consistent appreciation
 483 of the entire Martian atmosphere?

484 Figures 12 and 13 display the global average of the different fields of H₂O and HDO
 485 vapor mixing ratio and D/H over both hemispheres compared to the GCM outputs ob-
 486 tained for the reference simulation with the ACS sampling respectively at 80 km and 50 km
 487 altitude. Figure 12 shows that at 80 km, although the GCM reproduces the two peaks
 488 of water vapor corresponding to the two peaks of dust opacity of MY34 near $L_s \sim 190^\circ$
 489 and $L_s \sim 320^\circ$, it fails to simulate the increase of water vapor occurring near perihelion
 490 in both hemispheres, its intensity being much higher in the southern hemisphere. We

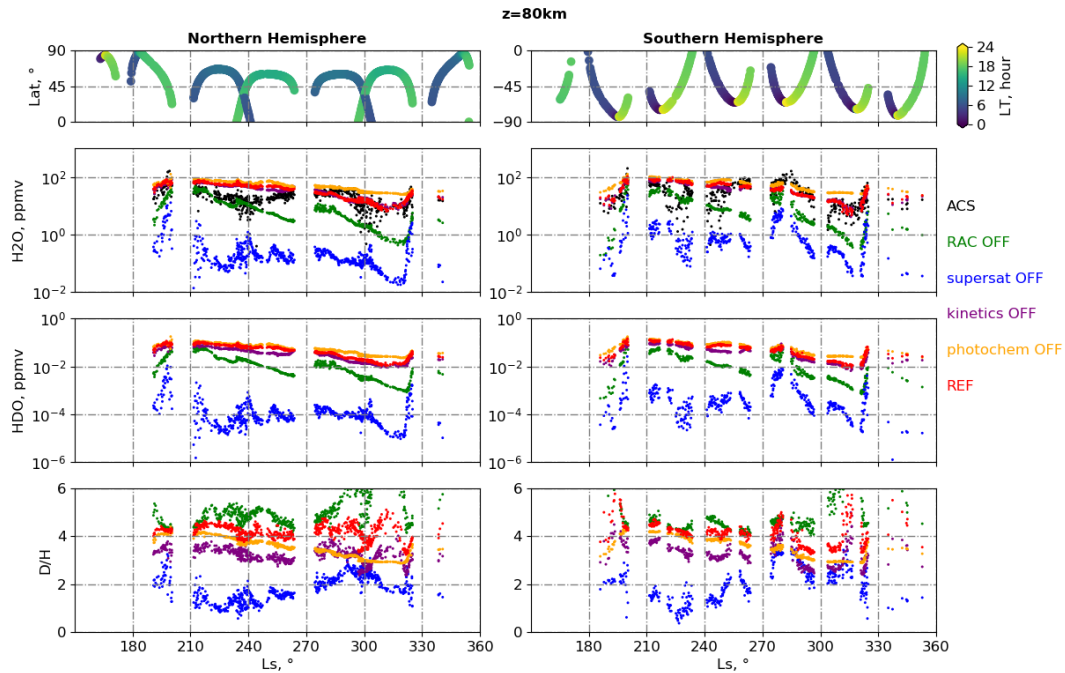


Figure 11. H_2O , HDO and D/H ratio GCM outputs interpolated to the ACS spatial and temporal coordinates at 80 km altitude, as a function of solar longitude (L_s). Left column: northern hemisphere, right column: southern hemisphere. First panel corresponds to the data coverage in latitude and local time. Second row displays the H_2O volume mixing ratio in logarithmic scale. Third row displays the HDO volume mixing ratio in logarithmic scale. Fourth row contains the D/H ratio. GCM outputs are shown for the reference simulation [REF], a simulation in which the supersaturation has been turned off [supersat OFF], a simulation in which the radiative effect of clouds has been turned off [RAC OFF], a simulation in which the effect of kinetics has been turned off [kinetics OFF] and a simulation in which the photochemistry has been turned off [photochem OFF]. ACS water vapor volume mixing ratio are shown in the second row (black dots).

491 also remark the decrease of water vapor around $L_s=240^\circ$ and $L_s=300^\circ$, which are not
 492 reproduced by the model. As described in Section 4 before, the decrease of water vapor
 493 observed between $L_s\sim 210^\circ$ and $L_s\sim 270^\circ$ can be correlated with the presence of wa-
 494 ter ice clouds not reproduced by the model, because of the lack of dust nuclei transported
 495 to these upper altitude ranges. The absence of the peak observed around perihelion in
 496 the model can also be attributed to the misrepresentation of the dust vertical distribu-
 497 tion, as strong convection transports dust that warms higher altitude and therefore al-
 498 lows water penetration to higher altitude. At 50 km, on the other hand, the model seems
 499 to reproduce the observed tendency, except near the perihelion in the southern hemisphere,
 500 for the same reasons as at 80 km.

501 Figure 12 reveals that the ACS sampling is representative of the global behaviour
 502 of the atmosphere at 80 km, where the red dots and the blue line follow each other. This
 503 is not the case at 50 km, where strong deviations between ACS sampling and global av-
 504 erage can be seen. Indeed, the latitudinal coverage of the sampling easily explains the
 505 variability of the fields in comparison to the global average over each hemisphere, and
 506 we can observe that the water vapor amount at this altitude is increasing with decreas-
 507 ing latitudes. In particular D/H variation appears tightly correlated to the latitudinal
 508 sampling. The difference with the global average increases when the sampling approaches
 509 the poles, for example in the northern hemisphere between $L_s\sim 340^\circ$ and $L_s\sim 350^\circ$,
 510 where the D/H of the sampling reaches the value of $5\times\text{VSMOW}$, whereas it slowly de-
 511 creases in the global average around $3.6\times\text{VSMOW}$. The steep increase near both poles
 512 disappears, when turning the photochemistry off, which suggests it is due to fraction-
 513 ation by photolysis. As mentioned before, this is the direct effect of sampling near the
 514 equinox and the poles, where the air of the descending branch of the Hadley cell comes
 515 from the thermosphere, where photodissociation strongly operates.

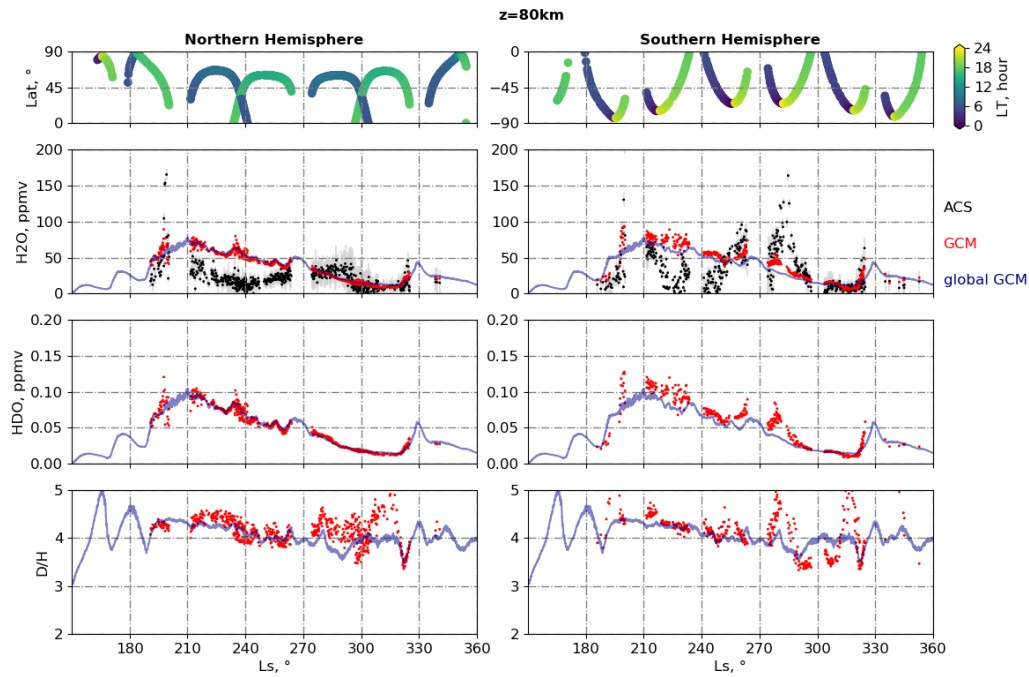


Figure 12. H_2O , HDO and D/H ratio GCM outputs interpolated to the ACS spatial and temporal coordinates at 80 km altitude, and globally averaged over each hemisphere, as a function of altitude and solar longitude (L_s). Left column: northern hemisphere, right column: southern hemisphere. First panel corresponds to the data coverage in latitude and local time. Second row displays the H_2O volume mixing ratio. Third row displays the HDO volume mixing ratio. Fourth row contains the D/H ratio. GCM outputs are shown for the reference simulation [REF] with GCM outputs interpolated to ACS coordinates (red dots), and for the global (zonal and latitudinal) average over each hemisphere (dark blue line). ACS water vapor volume mixing ratio are shown in the second row (black dots).

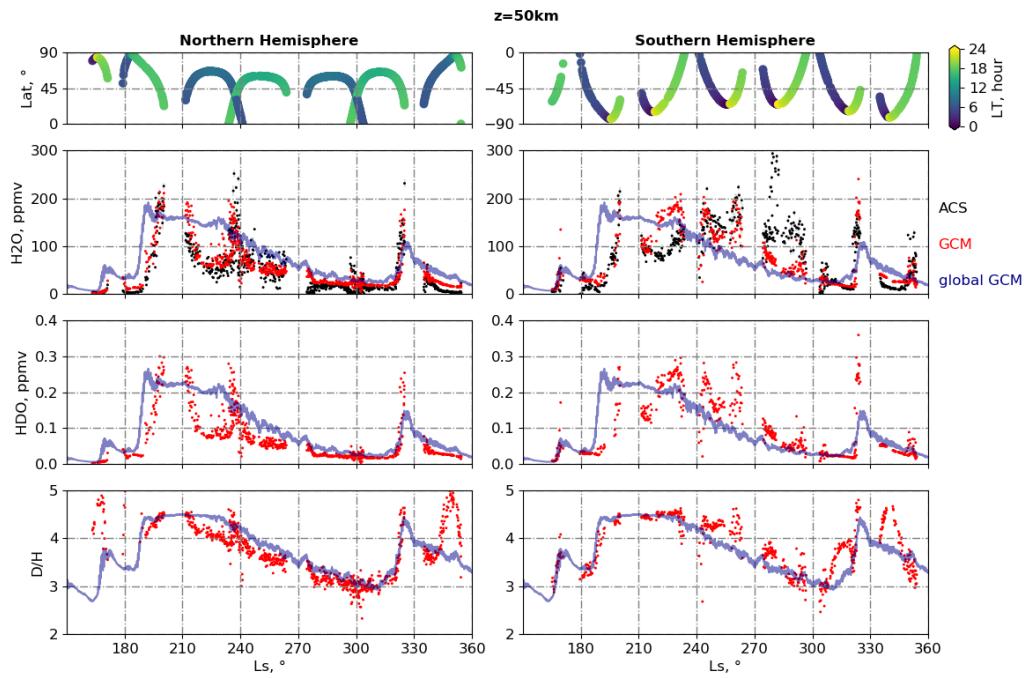


Figure 13. Same layout as Figure 12 at 50 km altitude

516

7 Conclusion

517

518

519

520

521

522

523

524

525

526

527

528

529

530

In this work we have shown the importance of modeling the detailed aspects of the water cycle to correctly account for the D/H cycle and, consequently, for the amount of water potentially escaping from the upper atmosphere. In particular, simulations with the LMD Mars GCM have shown that the radiative effect of clouds and their microphysics tend both to rise the altitude of the hygropause and the deuteropause, and significantly increase the D/H ratio in the middle atmosphere. In particular, the interaction between dust and water ice, responsible for the presence of supersaturation, tends to increase the porosity of the hygropause and deuteropause, allowing water (between 30 to 100 ppm) to penetrate higher altitude ranges (up to 100 km). The implementation of the effect of kinetics in the process of fractionation by condensation has also shown a significant difference in the D/H ratio, correlated with strong saturation. To conclude, supersaturation has two main impacts on the D/H, first by allowing a significant amount of water and HDO vapor to penetrate the upper atmosphere, and second by moderating the process of fractionation by condensation through the effect of kinetics.

531

532

533

534

535

536

537

538

539

540

541

542

The comparison between the TGO/ACS measurements of MY34 and the corresponding GCM outputs reveals a slight overestimation of the water vapor amount of the model in the middle-to-upper atmosphere, where water is in supersaturated state. This overestimation of supersaturation is suspected to result from a lack of dust nuclei present in the upper atmosphere, consequence of the misdealing of the vertical distribution of dust by the model. Supersaturation is also very sensitive to the poorly known "contact parameter" of the condensation nuclei, which is fixed in the model (see Navarro et al. (2014)). Besides, the model fails to represent the large increase of water vapor observed near to the perihelion in the Southern Hemisphere. This could also be attributed to the difficulty to represent the dust vertical distribution, supposed to be particularly controlled by vertical convection mechanisms during the dusty season. Further comparisons between GCM simulations and TGO/ACS observations have also confirmed the importance in

543 representing supersaturation to correctly account for the water vapor amount present
544 in the middle-to-upper atmosphere.

545 Finally, this study reveals that the TGO/ACS sampling is quite representative for
546 the global behavior of the atmosphere at high altitude levels (~ 80 km), except near the
547 poles, but the agreement is degraded in the middle altitude levels (~ 50 km), especially
548 near the poles.

549 Comparisons of the measured D/H profiles by TGO/ACS and the GCM are stud-
550 ied in the companion paper of Rossi et al. 2022 (this issue). In the near future, the fate
551 of deuterium on Mars will be studied with our GCM by means of a comprehensive de-
552 scription of the deuterium photochemistry and escape. These recent improvements bring
553 us closer fully representing the global D/H cycle, from the surface up to the top of the
554 atmosphere.

555 Acknowledgments

556 ExoMars is the space mission of ESA and Roscosmos. The ACS experiment is led by IKI
557 Space Research Institute in Moscow. The project acknowledges funding by Roscosmos
558 and CNES. Science operations of ACS are funded by Roscosmos and ESA.

559 The data used to produce the figures presented in this article can be obtained on
560 the following link : <https://doi.org/10.14768/9ba77f68-29a3-4bd6-8966-0900e2316a54>
561 The MRO/MCS dust opacity data were provided by Luca Montabone and are available
562 at the same link. The TGO/ACS/NIR temperature and water retrievals used in this study
563 were initially published in Fedorova et al. (2020) and are available at [http://exomars
564 .cosmos.ru/ACS_Results_stormy_water_vREzUd4pxG/](http://exomars.cosmos.ru/ACS_Results_stormy_water_vREzUd4pxG/). The TGO/ACS/TIRVIM and
565 TGO/ACS/NIR water ice retrievals were initially published in Luginin et al. (2020) and
566 can be obtained at <https://data.mendeley.com/datasets/rkszdmpdcy/1>. The LMD
567 General Circulation Model is available on request from the LMD team.

568 We thank the TGO/ACS team, so as Luca Montabone, for treating and provid-
569 ing the data with valuable inputs. We also thank the LMD team, in particular Antoine
570 Bierjon, for providing the tools to correctly handle with the model outputs.

571 M.V. acknowledges support from the DIM ACAV labelled by the Ile-de-France re-
572 gion in support for the research (Domaine d'Intérêt Majeur, Astrophysique et Conditions
573 d'Apparition de la Vie)". L.R. acknowledges support from CNES.

574 References

- 575 Alday, J., Trokhimovskiy, A., Irwin, P. G. J., Wilson, C. F., Montmessin, F.,
576 Lefèvre, F., ... Shakun, A. (2021a). Isotopic fractionation of water and its
577 photolytic products in the atmosphere of Mars. *Nature Astronomy*. doi:
578 10.1038/s41550-021-01389-x
- 579 Alday, J., Trokhimovskiy, A., Irwin, P. G. J., Wilson, C. F., Montmessin, F.,
580 Lefèvre, F., ... Shakun, A. (2021b). Isotopic fractionation of water and its
581 photolytic products in the atmosphere of Mars. *Nature Astronomy*, 5. doi:
582 10.1038/s41550-021-01389-x
- 583 Angelats i Coll, M., Forget, F., López-Valverde, M. A., & González-Galindo, F.
584 (2005). The first Mars thermospheric general circulation model: The Martian
585 atmosphere from the ground to 240 km. *Geophys. Res. Lett.*, 32, 4201. doi:
586 10.1029/2004GL021368
- 587 Belyaev, D. A., Fedorova, A. A., Trokhimovskiy, A., Alday, J., Montmessin, F., Ko-
588 rablev, O. I., ... Shakun, A. V. (2021). Revealing a High Water Abundance
589 in the Upper Mesosphere of Mars With ACS Onboard TGO. *Geophysical
590 Research Letters*, 48(10). doi: 10.1029/2021GL093411

- 591 Bertaux, J.-L., & Montmessin, F. (2001). Isotopic fractionation through water vapor
592 condensation: The deuteropause, a cold trap for deuterium in the atmosphere
593 of mars. *Journal of Geophysical Research: Planets*, 106(E12), 32879-32884.
594 doi: 10.1029/2000JE001358
- 595 Chaufray, J. Y., Mayyasi, M., Chaffin, M., Deighan, J., Bhattacharyya, D.,
596 Clarke, J., ... Jakosky, B. (2021). Estimate of the D/H Ratio in the
597 Martian Upper Atmosphere from the Low Spectral Resolution Mode of
598 MAVEN/IUVS. *Journal of Geophysical Research (Planets)*, 126(4), e06814.
599 doi: 10.1029/2020JE006814
- 600 Cheng, B.-M., Chew, E. P., Liu, C.-P., Bahou, M., Lee, Y.-P., Yung, Y. L., & Ger-
601 stell, M. F. (1999). Photo-induced fractionation of water isotopomers in the
602 martian atmosphere. *Geophysical Research Letters*, 26(24), 3657-3660. doi:
603 10.1029/1999GL008367
- 604 Cheng, B.-M., Chung, C.-Y., Bahou, M., Lee, Y.-P., Lee, L. C., van Harreveld, R., &
605 van Hemert, M. C. (2004). Quantitative spectroscopic and theoretical study
606 of the optical absorption spectra of H₂O, HOD, and D₂O in the 125-145 nm
607 region. *Journal of Chemical Physics*, 120(1), 224-229. doi: 10.1063/1.1630304
- 608 Chung, C.-Y., Chew, E. P., Cheng, B.-M., Bahou, M., & Lee, Y.-P. (2001). Tem-
609 perature dependence of absorption cross-section of H₂O, HOD, and D₂O in
610 the spectral region 140-193 nm. *Nuclear Instruments and Methods in Physics
611 Research A*, 467(2002), 1572-1576. doi: 10.1016/S0168-9002(01)00762-8
- 612 Clarke, J. T., Bertaux, J. L., Chaufray, J. Y., Gladstone, G. R., Quemerais, E., Wil-
613 son, J. K., & Bhattacharyya, D. (2014, November). A rapid decrease of the
614 hydrogen corona of Mars. *grl*, 41(22), 8013-8020. doi: 10.1002/2014GL061803
- 615 Daerden, F., Whiteway, J. A., Neary, L., Komguem, L., Lemmon, M. T., Heav-
616 ens, N. G., ... Smith, M. D. (2015). A solar escalator on Mars: Self-
617 lifting of dust layers by radiative heating. *grl*, 42(18), 7319-7326. doi:
618 10.1002/2015GL064892
- 619 Encrenaz, T., DeWitt, C., Richter, M. J., Greathouse, T. K., Fouchet, T.,
620 Montmessin, F., ... Sagawa, H. (2018). New measurements of d/h on mars
621 using exes aboard sofia. *A&A*, 612, A112. doi: 10.1051/0004-6361/201732367
- 622 Fedorova, A. A., Montmessin, F., Korablev, O., Luginin, M., Trokhimovskiy, A.,
623 Belyaev, D. A., ... Wilson, C. F. (2020). Stormy water on Mars: The distri-
624 bution and saturation of atmospheric water during the dusty season. *Science*,
625 367(6475), 297-300. doi: 10.1126/science.aay9522
- 626 Forget, F., Hourdin, F., Fournier, R., Hourdin, C., Talagrand, O., Collins, M., ...
627 Huot., J.-P. (1999). Improved general circulation models of the Martian atmo-
628 sphere from the surface to above 80 km. *J. Geophys. Res.*, 104, 24,155-24,176.
- 629 Gilli, G., Forget, F., Spiga, A., Navarro, T., Millour, E., Montabone, L., ...
630 Schofield, J. T. (2020). Impact of Gravity Waves on the Middle Atmosphere
631 of Mars: A Non-Orographic Gravity Wave Parameterization Based on Global
632 Climate Modeling and MCS Observations. *Journal of Geophysical Research
633 (Planets)*, 125(3), e05873. doi: 10.1029/2018JE005873
- 634 González-Galindo, F., Chaufray, J. Y., López-Valverde, M. A., Gilli, G., Forget,
635 F., Leblanc, F., ... Yagi, M. (2013). Three-dimensional Martian ionosphere
636 model: I. The photochemical ionosphere below 180 km. *Journal of Geophysical
637 Research (Planets)*, 118(10), 2105-2123. doi: 10.1002/jgre.20150
- 638 Heavens, N. G., Kass, D. M., & Shirley, J. H. (2019). Dusty Deep Convection in the
639 Mars Year 34 Planet-Encircling Dust Event. *Journal of Geophysical Research
640 (Planets)*, 124(11), 2863-2892. doi: 10.1029/2019JE006110
- 641 Heavens, N. G., Richardson, M. I., Kleinböhl, A., Kass, D. M., McCleese, D. J.,
642 Abdou, W., ... Wolkenberg, P. M. (2011). Vertical distribution of dust in
643 the Martian atmosphere during northern spring and summer: High-altitude
644 tropical dust maximum at northern summer solstice. *Journal of Geophysical
645 Research (Planets)*, 116(E15), E01007. doi: 10.1029/2010JE003692

- 646 Jouzel, J., & Merlivat, L. (1984). Deuterium and oxygen 18 in precipitation: Mod-
 647 eling of the isotopic effects during snow formation. *jgr*, *89*(D7), 11,749-11,757.
 648 doi: 10.1029/JD089iD07p11749
- 649 Krasnopolsky, V. A. (2015). Variations of the hdo/h2o ratio in the martian atmo-
 650 sphere and loss of water from mars. *Icarus*, *257*, 377 - 386. doi: https://doi
 651 .org/10.1016/j.icarus.2015.05.021
- 652 Lamb, K. D., Clouser, B. W., Bolot, M., Sarkozy, L., Ebert, V., Saathoff, H.,
 653 ... Moyer, E. J. (2017). Laboratory measurements of hdo/h2o iso-
 654 topic fractionation during ice deposition in simulated cirrus clouds. *Pro-
 655 ceedings of the National Academy of Sciences*, *114*(22), 5612–5617. doi:
 656 10.1073/pnas.1618374114
- 657 Lefèvre, F., Trokhimovskiy, A., Fedorova, A., Baggio, L., Lacombe, G., Määttä-
 658 nen, A., ... Montmessin, F. (2021). Relationship Between the Ozone and Wa-
 659 ter Vapor Columns on Mars as Observed by SPICAM and Calculated by a
 660 Global Climate Model. *Journal of Geophysical Research (Planets)*, *126*(4). doi:
 661 10.1029/2021JE006838
- 662 Luginin, M., Fedorova, A., Ignatiev, N., Trokhimovskiy, A., Shakun, A., Grigoriev,
 663 A., ... Korablev, O. (2020). Properties of Water Ice and Dust Particles in
 664 the Atmosphere of Mars During the 2018 Global Dust Storm as Inferred From
 665 the Atmospheric Chemistry Suite. *Journal of Geophysical Research (Planets)*,
 666 *125*(11), e06419. doi: 10.1029/2020JE006419
- 667 Madeleine, J.-B., Forget, F., Millour, E., Montabone, L., & Wolff, M. J. (2011,
 668 November). Revisiting the radiative impact of dust on Mars using the LMD
 669 Global Climate Model. *Journal of Geophysical Research (Planets)*, *116*, 11010.
 670 doi: 10.1029/2011JE003855
- 671 Madeleine, J.-B., Forget, F., Millour, E., Navarro, T., & Spiga, A. (2012). The
 672 influence of radiatively active water ice clouds on the Martian climate. *Geo-
 673 phys. Res. Lett.*, *39*, 23202. doi: 10.1029/2012GL053564
- 674 Maltagliati, L., Montmessin, F., Fedorova, A., Korablev, O., Forget, F., & Bertaux,
 675 J.-L. (2011, September). Evidence of Water Vapor in Excess of Saturation in
 676 the Atmosphere of Mars. *Science*, *333*, 1868-. doi: 10.1126/science.1207957
- 677 Merlivat, L., & Nief, G. (1967). Fractionnement isotopique lors des changements
 678 d'état solide-vapeur et liquide-vapeur de l'eau à des températures inférieures à
 679 0°C. *Tellus*, *19*(1), 122-127. doi: 10.1111/j.2153-3490.1967.tb01465.x
- 680 Montabone, L., Forget, F., Millour, E., Wilson, R. J., Lewis, S. R., Cantor, B., ...
 681 Wolff, M. J. (2015). Eight-year climatology of dust optical depth on Mars.
 682 *Icarus*, *251*, 65-95. doi: 10.1016/j.icarus.2014.12.034
- 683 Montabone, L., Spiga, A., Kass, D. M., Kleinböhl, A., Forget, F., & Millour,
 684 E. (2020). Martian year 34 column dust climatology from mars climate
 685 sounder observations: Reconstructed maps and model simulations. *Jour-
 686 nal of Geophysical Research: Planets*, *n/a*(n/a), e2019JE006111. doi:
 687 10.1029/2019JE006111
- 688 Montmessin, F., Fouchet, T., & Forget, F. (2004). Modeling the annual cycle of
 689 HDO in the Martian atmosphere. *Journal of Geophysical Research, Submitt-
 690 ed.*
- 691 Montmessin, F., Rannou, P., & Cabane, M. (2002). New insights into Martian dust
 692 distribution and water-ice cloud microphysics. *Jour. Geophys. Res. (Planets)*,
 693 4-1.
- 694 Navarro, T., Madeleine, J.-B., Forget, F., Spiga, A., Millour, E., Montmessin, F., &
 695 Määttä-
 696 nen, A. (2014). Global Climate Modeling of the Martian water cycle
 697 with improved microphysics and radiatively active water ice clouds. *Journal of
 698 Geophysical Research (Planets)*. doi: 10.1002/2013JE004550
- 699 Neary, L., Daerden, F., Aoki, S., Whiteway, J., Clancy, R. T., Smith, M., ... Van-
 700 daele, A. C. (2020). Explanation for the Increase in High-Altitude Water on
 Mars Observed by NOMAD During the 2018 Global Dust Storm. *Geophysical*

- 701 *Research Letters*, 47(7), e84354. doi: 10.1029/2019GL084354
- 702 Owen, T., Maillard, J. P., de Bergh, C., & Lutz, B. L. (1988). Deuterium on Mars:
703 The Abundance of HDO and the Value of D/H. *Science*, 240(4860), 1767-
704 1770. doi: 10.1126/science.240.4860.1767
- 705 Risi, C., Bony, S., Vimeux, F., & Jouzel, J. (2010). Water-stable isotopes in the
706 LMDZ4 general circulation model: Model evaluation for present-day and
707 past climates and applications to climatic interpretations of tropical isotopic
708 records. *Journal of Geophysical Research (Atmospheres)*, 115, D12118. doi:
709 10.1029/2009JD013255
- 710 Rossi, L., Vals, M., Montmessin, F., Forget, F., Millour, E., Fedorova, A., ... Ko-
711 rablev, O. (2021). The Effect of the Martian 2018 Global Dust Storm on
712 HDO as Predicted by a Mars Global Climate Model. *grl*, 48(7), e90962. doi:
713 10.1029/2020GL090962
- 714 Spiga, A., Faure, J., Madeleine, J.-B., Määttänen, A., & Forget, F. (2013, April).
715 Rocket dust storms and detached dust layers in the Martian atmosphere. *Jour-
716 nal of Geophysical Research (Planets)*, 118, 746-767. doi: 10.1002/jgre.20046
- 717 Stcherbinine, A., Vincendon, M., Montmessin, F., Wolff, M. J., Korablev, O., Fe-
718 dorova, A., ... Shakun, A. (2020, March). Martian Water Ice Clouds During
719 the 2018 Global Dust Storm as Observed by the ACS-MIR Channel Onboard
720 the Trace Gas Orbiter. *Journal of Geophysical Research (Planets)*, 125(3),
721 e06300. doi: 10.1029/2019JE006300
- 722 Urata, R. A., & Toon, O. B. (2013). Simulations of the martian hydrologic cycle
723 with a general circulation model: Implications for the ancient martian climate.
724 *Icarus*, 226, 229-250. doi: 10.1016/j.icarus.2013.05.014
- 725 Vandaele, A. C., Korablev, O., Daerden, F., Aoki, S., Thomas, I. R., Altieri, F., ...
726 Zorzano, M. P. (2019). Martian dust storm impact on atmospheric H₂O and
727 D/H observed by ExoMars Trace Gas Orbiter. *Nature*, 568(7753), 521-525.
728 doi: 10.1038/s41586-019-1097-3
- 729 Villanueva, G., Liuzzi, G., Crismani, M. M. J., Aoki, S., Vandaele, A. C., Daer-
730 den, F., ... NOMAD team (2021). Water heavily fractionated as it as-
731 cends on Mars as revealed by ExoMars/NOMAD. *Science Advances*. doi:
732 10.1126/sciadv.abc8843
- 733 Villanueva, G. L., Mumma, M. J., Novak, R. E., Käufel, H. U., Hartogh, P., Encre-
734 naz, T., ... Smith, M. D. (2015). Strong water isotopic anomalies in the mar-
735 tian atmosphere: Probing current and ancient reservoirs. *Science*, 348(6231),
736 218-221. doi: 10.1126/science.aaa3630
- 737 Wang, C., Forget, F., Bertrand, T., Spiga, A., Millour, E., & Navarro, T. (2018).
738 Parameterization of Rocket Dust Storms on Mars in the LMD Martian GCM:
739 Modeling Details and Validation. *Journal of Geophysical Research (Planets)*,
740 123(4), 982-1000. doi: 10.1002/2017JE005255
- 741 Yung, Y. L., Wen, J.-S., Pinto, J. P., Allen, M., Pierce, K. K., & Paulson, S. (1988).
742 HDO in the Martian atmosphere: Implications for the abundance of crustal
743 water. *Icarus*, 76(1), 146-159. doi: 10.1016/0019-1035(88)90147-9